small methods
www.small-methods.com

Mitochondrial STED Imaging and Membrane Potential Monitoring with a Cationic Molecular Probe

Lu Gao, Rana Dalapati, Beibei Gao, Xiaoyu Huang, Dan Zhao, Fu Wang, and Ling Zang**

Mitochondria are essential organelles that not only undergo dynamic morphological changes but also exhibit functional activities such as mitochondrial membrane potential (MMP). While super-resolution techniques such as stimulated emission depletion (STED) nanoscopy can visualize the ultrastructure of mitochondria and the MMP probe can monitor mitochondria function, few dyes meet both demands. Here, a small molecule (MitoPDI-90) based on perylene diimide with cationic groups is reported and used for mitochondrial STED imaging and MMP indication. Characterized by excellent photostability, biocompatibility, and high quantum yield, MitoPDI-90 exhibits STED imaging compatibility, facilitating visualization of mitochondrial cristae and time-lapse imaging of highly dynamic mitochondria in living cells. Besides, MitoPDI-90 targets the mitochondria through electrical potential, also enabling live-cell MMP monitoring. MitoPDI-90 allows for super-resolution visualization and time-lapse imaging of mitochondria, and more importantly, indication of changes in MMP, providing insight into the functional activity of live-cell mitochondria.

1. Introduction

Mitochondria are vital organelles serving as cell powerhouses, facilitating eukaryotic cell metabolism, apoptosis, and energy production.[1] The mitochondria are characterized by a double-membrane structure comprising an inner membrane (IM) and outer membrane, each serving distinct functions and forming specialized regions.[2] Especially, due to the highly in-folded IM, the membrane ultrastructures called cristae as formed are densely stacked in proximity with a distance below 100 nm in many mammalian cells.[2–4] Mitochondrial cristae occupy the majority of the inner membrane surface and are the main site for energy exchange, therefore their morphological changes are closely related to mitochondrial function and cellular status.[3] In addition, the primary function of mitochondria is to produce adenosine triphosphate through oxidative phosphorylation, which occurs within the IM via mitochondrial membrane potential (MMP).[3] MMP can be derived from the electrochemical gradient across the IM and serves as a reliable readout of mitochondrial function, playing a crucial role in regulating and controlling mitochondrial cycles.[5–8] Thus, the cristae and MMP are both vital indicators of mitochondrial vitality, providing structural and functional insights into mitochondria, respectively.[5–8]

However, simultaneous visualization of mitochondrial cristae and MMP proves challenging. The diffraction limitation hinders traditional optical microscopies from distinguishing the mitochondrial cristae.[4] Previously, electron microscopy was commonly used to observe mitochondrial cristae in fixed specimens,[4,9] limiting the analysis of morphological changes such as fusion and fission in living cells.[5] Recently, super-resolution fluorescence microscopy, especially stimulated emission depletion (STED) microscopy and structure illumination microscopy (SIM),[4,10–13] have been successfully employed in nanoscale imaging of cristae and visualization of mitochondrial dynamics in living cells. In general, the SIM reconstructs super-resolution images through image processing, however, there are often artifacts and the risk of distortions in the reconstruction process. In comparison, STED microscopy directly acquires super-resolution images through point-scanning imaging, providing superior resolution and rapid imaging. Consequently, when conducting dynamic super-resolution imaging of live-cell mitochondria, particularly their inner cristae structure, STED imaging is far more visually intuitive and authentic compared to SIM.[4,14]

The resolution of STED imaging is related to the power of the depletion laser, relying on the brightness and photostability of fluorescence probes.[15–17] In the last decades, fluorescent probes used in living cells mainly include fluorescent proteins,

L. Gao, B. Gao, X. Huang, F. Wang
Med-X Research Institute and School of Biomedical Engineering
Shanghai Jiao Tong University
Shanghai 200240, China
E-mail: wangfu@sjtu.edu.cn
R. Dalapati, L. Zang
Department of Materials Science and Engineering
University of Utah
Salt Lake City, UT 84112, USA
E-mail: lzang@eng.utah.edu
D. Zhao
School of Environmental Science and Engineering
Shanghai Jiao Tong University
Shanghai 200240, China
The ORCID identification number(s) for the author(s) of this article can be found under https://doi.org/10.1002/smtd.202400525

DOI: 10.1002/smtd.202400525

organic molecules, aggregation-induced emission luminogens, and quantum dots.[18,19] Among them, the organic molecules are the main probes used in live-cell STED imaging due to their superior brightness and biocompatibility. Previously developed probes such as 10-*N*-nonyl acridine orange (NAO),[20] DTPAP-P,[21] MitoEsq-635,[10] MitoPB yellow,[9] and PKMO[22] have achieved the STED imaging of mitochondria in living cells. Unfortunately, these dyes focus on mitochondrial structure imaging and lack significant voltage sensitivity, making them difficult to be MMP probes.[23] The commonly used dyes for MMP monitoring include two common types: bicolor dyes such as tetrachlorotetraethyl benzimidazole carbocyanine iodine compounds, known as JC-1, which measure changes in MMP proportionately, and cationic dyes like rhodamine 123 (Rho123) and tetramethylrhodamine methyl ester (TMRM), which track changes in MMP through steady-state emission intensity changes.[6,8,24] However, these MMP probes have rarely been reported for STED imaging, possibly due to a lack of mitochondrial membrane structure dependence compared to other mitochondrial STED probes (like NAO), as well as issues such as insufficient photostability.[25] Therefore, probes used for mitochondrial imaging often struggle to balance charge sensitivity and membrane targeting, such as those with high voltage sensitivity, which makes it difficult to achieve STED super-resolution imaging or those with good membrane targeting but are unable to be voltage sensitive. So far, except for using NAO and tetramethylrhodamine ethyl ester (TMRE) to achieve MMP STED imaging and Airy imaging of mitochondria,[20] there have been limited reports on the mitochondrial probes for STED imaging to monitor MMP in living cells with super-resolution. Thus, the development of probes for mitochondrial STED imaging and MMP monitoring in living cells remains a continuous effort.

Among numerous dyes, organic small molecules based on the rigid structure of perylene-3,4,9,10-tetracarboxylic diimide (PDI) have the potential to achieve STED imaging and MMP monitoring. PDIs form a unique class of fluorophores with high thermal and photo-stability, and tunable optical and electronic properties that are suitable for varying applications in optoelectronics such as light-emitting diodes, photovoltaics, sensors, as well as bioimaging.[26,27] PDI offers high structural flexibility for side group modification at both the imide and bay positions,[28,29] which in turn helps tune not only the optical properties (e.g., absorption and fluorescence) but also the cytotoxicity to make the dye best fit for cell imaging. Particularly, tuning the fluorescence emission up to the long wavelength region helps enhance the optical penetration in bio-species, highly favorable for cell imaging as well. Substituent modification of PDI with cationic groups, such as triphenylmethylphosphonium, Tetraphenylphosphonium, dequalinium, and quaternary ammonium salts, would facilitate the molecules to target and enter the IM of mitochondria via electrostatic potential.[30,31] In this way, PDI can be endowed with the ability to monitor MMP. In this regard, cationic PDIs could serve as ideal fluorophore candidates for STED imaging and MMP monitoring of mitochondria.

Herein, we report on a cationic PDI fluorophore, MitoPDI-90, which is based on a tetrachord-substituted PDI backbone. MitoPDI-90 meets the primary functional requirements for STED imaging, specifically targeting mitochondria for visualization of MMP change. As shown in this study, MitoPDI-90 can easily penetrate cells and display superior targeting capability toward mitochondria enabling visualization of cristae. Compared to bright MMP probes such as Rho123 and TMRM, MitoPDI-90 still has a relatively weaker fluorescence intensity even with a quantum yield of ≈62%. At the same concentration and optimal excitation, the maximum fluorescence intensity of MitoPDI-90 is only ≈40% of Rho123 and 8% of TMRM. However, MitoPDI-90 not only demonstrates MMP monitoring but also super-resolution imaging under STED microscopy, enabling monitoring of mitochondrial dynamics in living cells. We anticipate that MitoPDI-90 has the potential to be developed as an excellent mitochondrial probe for super-resolution structure and functional MMP imaging.

2. Results and Discussion

2.1. Design of Fluorescent Mitochondrial Probe with High Photostability

As illustrated in **Figure 1**, the photostable dye MitoPDI-90 is based on a tetrachloro-substituted PDI backbone with the two imide side chains modified with quaternary ammonium ions. The cationic modification renders the water solubility of the molecule, while the tetrachloro-substitution causes significant twisting of the PDI backbone, which is intrinsically planar before being substituted with the chlorines. Moreover, the quaternary ammonium cations enable the dye to target mitochondria and monitor MMP. The twisted conformation hinders the $\pi-\pi$ stacking interaction (aggregation) between the PDI planes,[28,32] thus enhancing the molecular dispersion of PDI when dissolved in solution. The molecular dispersion of fluorophores is conducive to maximizing the fluorescence emission. Indeed, the fluorescence quantum yield of MitoPDI-90 in water solution was determined in this study to be as high as 62%. In contrast, for the PDI fluorophore modified with the same cationic side chains but without modification at the bay area (PDI-68, Figure 1a), the fluorescence was found significantly weak, with a quantum yield of only 15%. This is mainly due to the $\pi-\pi$ stacking of PDI cores, a typical phenomenon often referred to as aggregation-induced quenching.[32,33] An analog of PDI-68 was also synthesized with the cationic side chains increased in length from 3 to 4 carbons (PDI-82, Figure 1a), to enhance the flexibility and thereby the dispersion in water. However, the fluorescence quantum yield as measured for PDI-82 was still as low as 15%, implying that the side chain modification at imide positions does not seem to help much the molecular dispersion in water, which is otherwise more dependent on the structural modification at the bay area. Therefore, MitoPDI-90 with a high quantum yield was selected as a fluorescence imaging probe. Detailed spectral and solubility characterizations of MitoPDI-90 are summarized in Figure 1b, Figures S1 and S2 (Supporting Information).

MitoPDI-90 exhibits an absorption maximum of ≈520 nm with a Stokes shift of ≈35 nm (Figure 1b). Within the range of 100 μM (in water), the UV absorption of MitoPDI-90 remains almost unchanged with increasing concentration, while the absorption intensity increases with increasing concentration (Figure S3b, Supporting Information). As the concentration increases, the fluorescence emission of the dye undergoes a slight

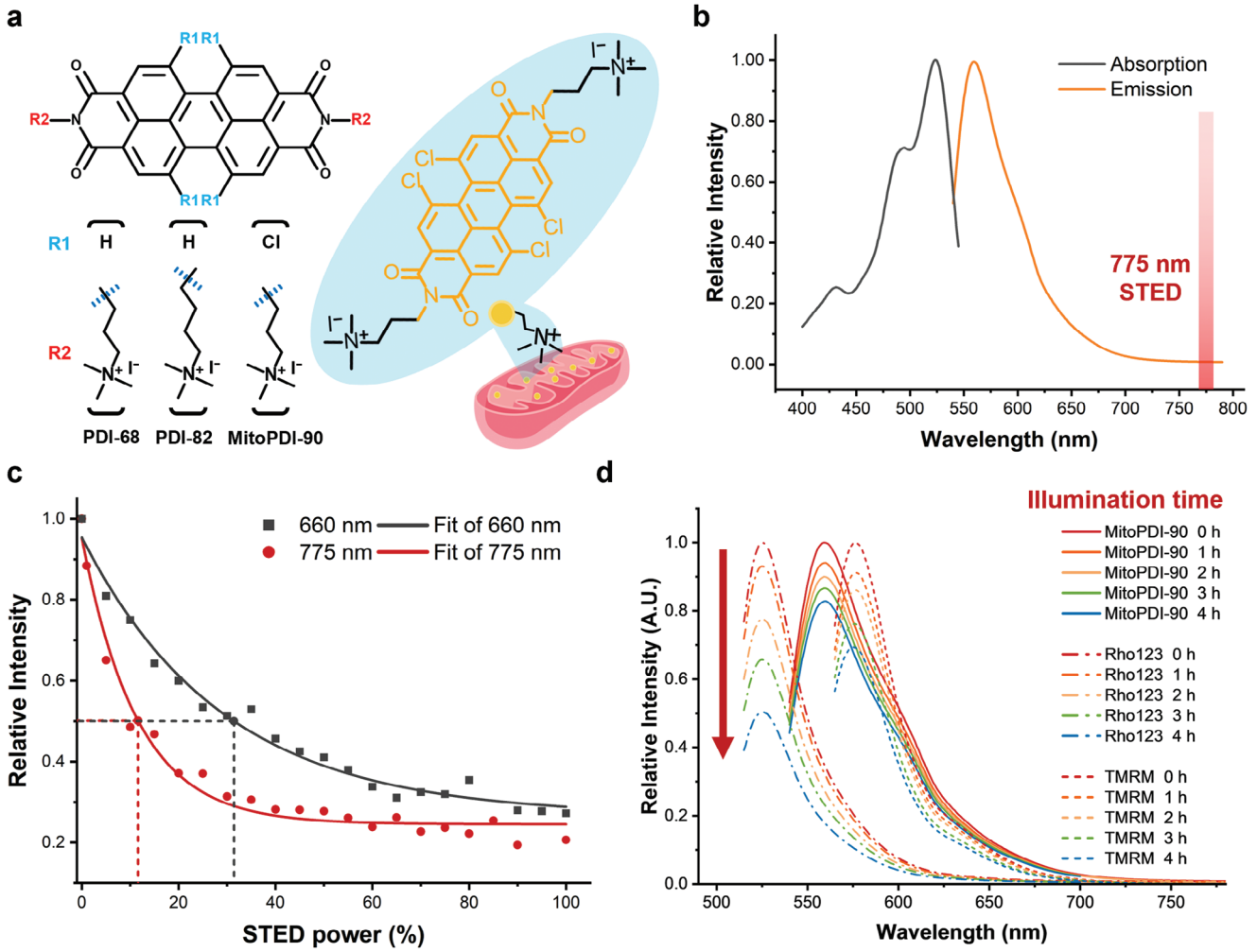

Figure 1. Properties of MitoPDI-90. a) Chemical structure of MitoPDI-90 in comparison with the analogues PDI-68 and PDI-82. b) Absorption and fluorescence (emission) spectra of the MitoPDI-90 (1 μM in water), indicating that a 775 nm pulse laser can be employed for depletion on the STED setup. c) The detected fluorescence signal measured from a MitoPDI-90 solution (1 μM in water) cast a coverslip as a function of the depletion beam intensity of two kinds of STED laser. The excitation beam was 520 nm with a frequency of 80 MHz, and the STED beam was 660 nm (continuous wave) and 775 nm (80 MHz pulse laser). d) Comparison of photobleaching resistance between MitoPDI-90, TMRM, and Rho123. The solutions of MitoPDI-90 (1 μM in water) and Rho123 (1 μM in water) with similar emission intensities were continuously illumination under a xenon lamp (50 W) for 4 h and the fluorescence spectra were measured every 1 h, respectively.

red shift (Figure S3b, Supporting Information). To verify the STED compatibility of MitoPDI-90, a depletion experiment of MitoPDI-90 solution (1 μM in water) was conducted. As shown in the solution depletion experiment, the saturation intensity of MitoPDI-90 under 775 nm laser is approximately three times lower than that under 660 nm (Figure 1c), which can be attributed to the fact that the 660 nm laser is a continuous wave, while the 775 nm laser is pulse mode. The result means the 775 nm laser could implement significant depletion under lower power than the 660 nm laser for STED imaging of MitoPDI-90, even though the wavelength is far from the emission peak of MitoPDI-90. Additionally, the photostability of STED dyes determines the image quality. As a representative of MMP dye, a cationic molecule dye Rho123 was selected as a reference. Compared with Rho123 and TMRM, MitoPDI-90 remained at least 80% fluorescence intensity after 4 h of continuous illumination of white light, exhibiting higher photostability than Rho123 and TMRM (Figure 1d) in water solution. The result indicates that under broad spectral irradiation, the aqueous solution of MitoPDI-90 exhibits better overall anti-photobleaching properties. Apparently, MitoPDI-90 is an ideal candidate for fluorescence imaging and MMP monitoring, which is worthy of being explored with super-resolution imaging on STED microscopy.

2.2. Live-Cell Mitochondria Confocal Imaging with MitoPDI-90

To investigate the mitochondrial targeting of MitoPDI-90, the mitochondrial dye Mitobright LT deep red (MBDR) was selected as a reference. Notably, MBDR is insensitive to MMP, enabling long-term stable imaging of mitochondria. Another attractive reason for choosing MBDR is that its fluorescence spectrum with an

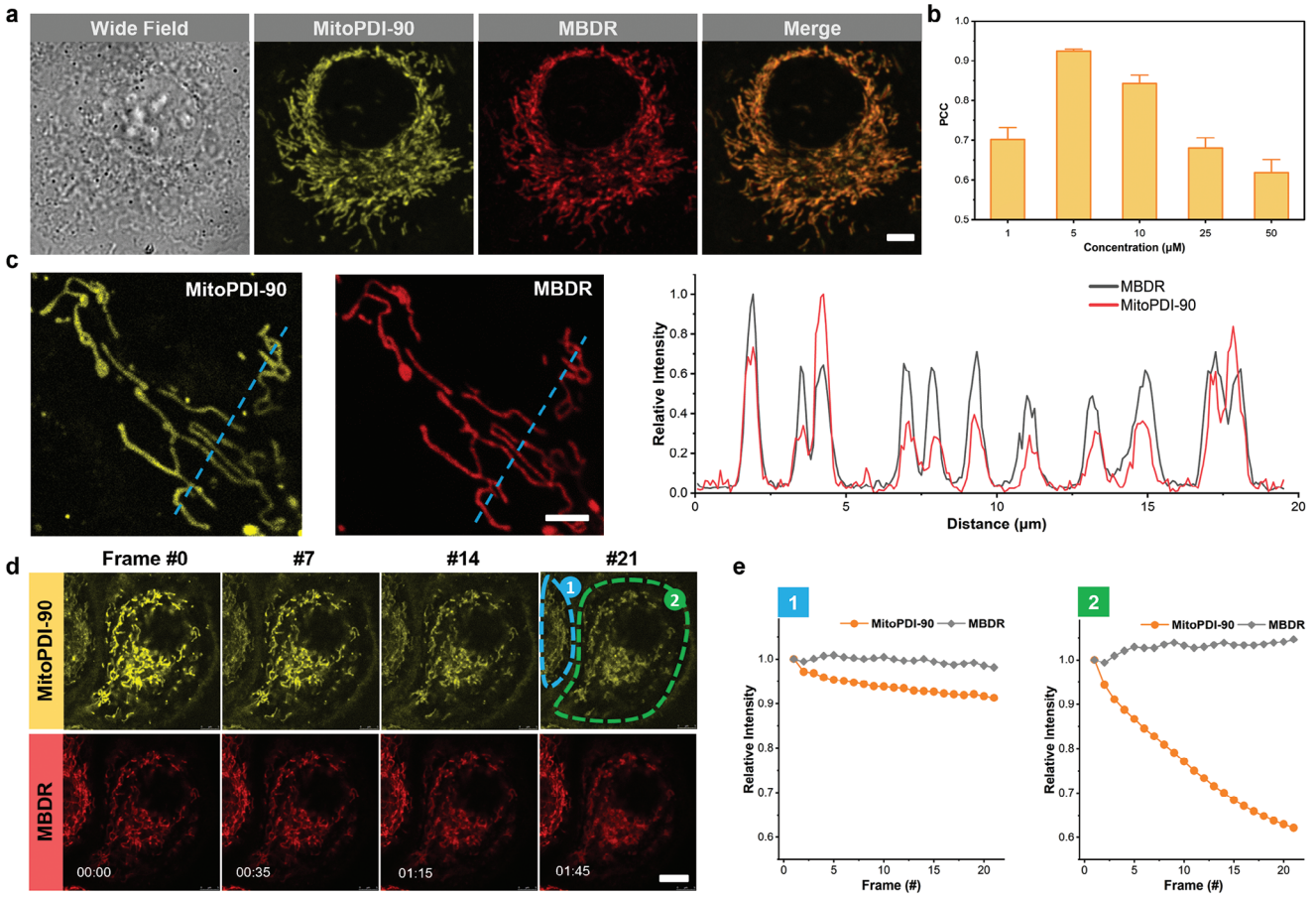

Figure 2. Analysis of mitochondrial imaging of MitoPDI-90. a) Co-localization confocal imaging of living cells stained with MitoPDI-90 (10 μM) and MBDR (0.1 μM). From left to right: wide field; MitoPDI-90 excited at 520 nm and collected at 540–620 nm; MBDR excited at 640 nm and collected at 655–700 nm; merged image. b) Co-localization confocal imaging of living cells stained with MitoPDI-90 (10 μM) and MBDR (0.1 μM) in the local area. The cross-section plot along the orange dashed lines in the two pictures is shown. c) Distribution of PCC between cell images stained with MBDR at 0.1 μM and MitoPDI-90 at various concentrations of 1, 5, 10, 25, and 50 μM. The bar and the whisker represent the mean ± SE, $n = 5$. d) Co-localization time-lapse confocal imaging of living cells stained with MitoPDI-90 (5 μM, upper row) and MBDR (0.1 μM, lower row). The blue and green dashed lines in the MitoPDI-90 image sequence select cells in normal and apoptotic states, respectively. e) The average fluorescence intensity of MitoPDI-90 and MBDR channels at the region of interest in d is plotted as a function of the recorded frame number. The graph on the left represents the blue selection area 1 in Frame #21 of d, and the right one is the green selection area 2 in Frame #21 of d. Scale bars in a, b, and d are 5 μm.

emission maximum of 650 nm does not overlap with MitoPDI-90, which can avoid interference in dual-color imaging.

The HeLa cells were co-stained with MBDR and MitoPDI-90 for colocalization analysis with confocal imaging (**Figure** 2a,c). The Pearson's correlation coefficient (PCC) of MitoPDI-90 and MBDR channels was employed as a quantification of co-localization efficiency to characterize the mitochondrial targeting performance of MitoPDI-90 (Figure S4, Supporting Information). To further optimize the targeting performance of MitoPDI-90, the PCC of HeLa cells co-stained with MBDR (0.1 μM) and MitoPDI-90 (at various concentrations of 1, 5, 10, 25, and 50 μM) (Figure 2b) was quantified. The results indicated that PCC remains at a high level above 0.9 with MitoPDI-90 at ≈5 μM, but gradually decreases with the concentration of MitoPDI-90 exceeding 10 μM. Despite that the fluorescence signal of MitoPDI-90 dye elevated with increasing concentration, the mitochondrial fluorescence intensity did not significantly enhance when the dose concentration was beyond ≈10 μM, as excessive dye could be engulfed by lysosomes, presenting strong fluorescence intensity groups with aggregates, resulting in decreased PCC. This was primarily due to the limited value of MMP,[8] and the positively charged MitoPDI-90 dye entering mitochondria would eventually reach its saturation state, reflecting an equilibrium determined by the limited number of local binding sites. Therefore, a concentration of ≈5 μM is considered the most suitable condition for MitoPDI-90 as used for mitochondrial imaging in this study.

Co-localization time-lapse imaging of HeLa cells stained with MBDR and MitoPDI-90 was employed to further explore the difference between MitoPDI-90 (as a functional probe) and MBDR (mainly as a structure probe). An in situ comparison of the two dyes was provided by a field of view including both normal and apoptotic cells (Figure 2d). In Figure 2d (Frame #21), a normal cell was selected as no.1 by the blue dashed line in the region of interest. The mitochondrial morphology of no.1 remained relatively unchanged throughout the imaging period, and the fluorescence intensities of MitoPDI-90 and MBDR also demonstrated

little variation. In contrast, an apoptotic cell identified by the green dashed line labeled as no. 2 exhibited a transformation in the morphology of its mitochondria, changing from tubular to spherical structures (Figure 2d; Video S1, Supporting Information). Both MitoPDI-90 and MBDR showed this morphological change synchronously during imaging, but MitoPDI-90 exhibited a significant change in fluorescence intensity (Figure 2e). Compared to normal cells, the mitochondria of apoptotic cells may differ in morphology and MMP, but cells stained with MBDR could only observe the former. Therefore, compared to MBDR, MitoPDI-90 enables the visualization of both mitochondrial morphology and MMP through fluorescence distribution and fluorescence intensity.

2.3. Live-Cell STED Imaging with MitoPDI-90

Considering the optical properties, a 520 nm excitation laser and a 775 nm STED laser were employed for STED imaging in living cells. Usually, the 775 nm laser caused less damage to cells compared with the STED lasers of shorter wavelengths such as 660 or 592 nm,[34] which would be beneficial to time-lapse imaging of living cells. Compared with confocal imaging, STED imaging provided more details on the distribution of MitoPDI-90 in living cells, including aggregates formed under high concentrations of dyes (**Figure 3**a) and the mitochondria morphology (Figure 3b). Notably, live-cell mitochondrial STED imaging achieved visualization of the spacing between mitochondria cristae with at least 81 nm (Figure 3b), providing more clear evidence of the binding site of MitoPDI-90. In contrast, the cationic probe TMRE used for MMP STED imaging achieved a resolution of ≈140 nm.[20] Therefore, MitoPDI-90, as an MMP dye, has demonstrated the resolution advantage of STED imaging. Results showed that the dye distribution within the mitochondria was not uniform, but related to the ultrastructure of the cristae, confirming the mitochondrial membrane structure binding of MitoPDI-90, despite its voltage-dependent binding. With this membrane binding property, MitoPDI-90 also possessed super-resolution imaging capability for mitochondrial structures, particularly the ultrastructure of the mitochondrial cristae.

The time-lapse STED imaging for mitochondria was employed to further demonstrate the imaging application of MitoPDI-90 (Video S2, Supporting Information). The changes in mitochondrial morphology in time-lapse imaging revealed mitochondria as highly dynamic structures that constantly evolve with fusion and fission in living cells (Figure 3c,d). The results also suggested mitochondrial heterogeneity within cells, where fusion and fission co-occurred, representing the equilibrium state of mitochondria in the cell.[6,35]

2.4. MMP Monitoring with MitoPDI-90

Encouraged by the excellent mitochondrial targeting feature of MitoPDI-90, HeLa cells were stained with MitoPDI-90 to assess MMP imaging performance. One prerequisite of fluorescent dye for both STED imaging and MMP monitoring is to maintain photostability, which plays a decisive role in time-lapse imaging and the evaluation of MMP changes. Usually, results from the fluorescence-based MMP probes are often misleading in MMP analysis due to photobleaching.[36] Therefore, Rho123 and TMRM, the common MMP probes, were also carried out with the same photostability test. The photobleaching resistance of the three dyes was compared under different exposure durations in living cells (Figure S5, Supporting Information). Since the point scanning mode is used by confocal microscopy, the exposure duration is the laser irradiation time per pixel, which is named the dwell time. Three dwell times of ≈1.5, 2.5, and 5 µs were taken to continuously scan 50 images of living cells stained with Rho123 (**Figure 4**a), MitoPDI-90 (Figure 4b), and TMRM (Figure 4c), respectively. After scanning 50 images continuously with a dwell time of 1.5 µs, MitoPDI-90 still maintained a fluorescence intensity of ≈90%, while Rho123 rapidly dropped to ≈60% and TMRM dropped to ≈75%. The results indicated that MitoPDI-90 showed better resistance to photobleaching than Rho123 and TMRM in time-lapse imaging of living cells. The result is also similar to the performance of the material in water solution, indicating that the cellular environment did not significantly affect the photobleaching resistance of MitoPDI-90. Particularly, the excellent photobleaching resistance brings more reliable MMP monitoring, which primarily relies on fluorescence intensity modulation.

In addition, based on the characteristics of MMP probes, it is necessary to clarify the quenching and non-quenching modes to correctly explain the changes in MMP.[37,38] Typically, Rho123 uses a quenching mode for imaging, which means using a high concentration (≈1.5 µM, followed by wash) of dye to form aggregates within mitochondria, thereby quenching the partial fluorescence emission of the aggregated dye. TMRM typically uses a non-quenching mode, which means using probes at lower concentrations (≈20 nM) and imaging with probes staying in the buffer. To evaluate the mode in which MitoPDI-90 works at the previously selected appropriate concentration (5 µM, followed by wash), 10 µM carbonyl cyanide 3-chlorophenylhydrazone (CCCP) was used to induce depolarization of mitochondria, and then compare the in situ responses of three dyes to MMP changes in their respective modes (Figure 4d). In the quenching mode of Rho123, the MMP collapse led to the release of dyes, which instantly increased fluorescence signals. In the nonquenching mode of TMRM, dyes in mitochondria did not aggregate or quench, which made relative static changes along with MMP loss. In contrast, MitoPDI-90 did not undergo aggregation quenching in mitochondria like Rho123, even at a concentration of 5 µM. By comparing the fluorescence emission spectra of Rho123, TMRM, and MitoPDI-90 at the same concentrations (1 µM in water), it can be found that one possible reason for the high incubation concentration of MitoPDI-90 is that its fluorescence emission intensity is lower than that of Rho123 and TMRM at the same concentration (Figure S6a, Supporting Information). Besides, the analysis of permeability across the plasma membrane of dyes was tested by comparing the fluorescence intensity of culture media containing different concentration dyes before and after cell incubation. It can be seen that the absorption of TMRM by cells is higher than that of MitoPDI-90 (Figure S6b, Supporting Information). The fluorescence intensity and cellular absorption of MitoPDI-90 are lower than those of TMRM at the same concentration, which may be the reason why MitoPDI-90 requires higher incubation concentrations.

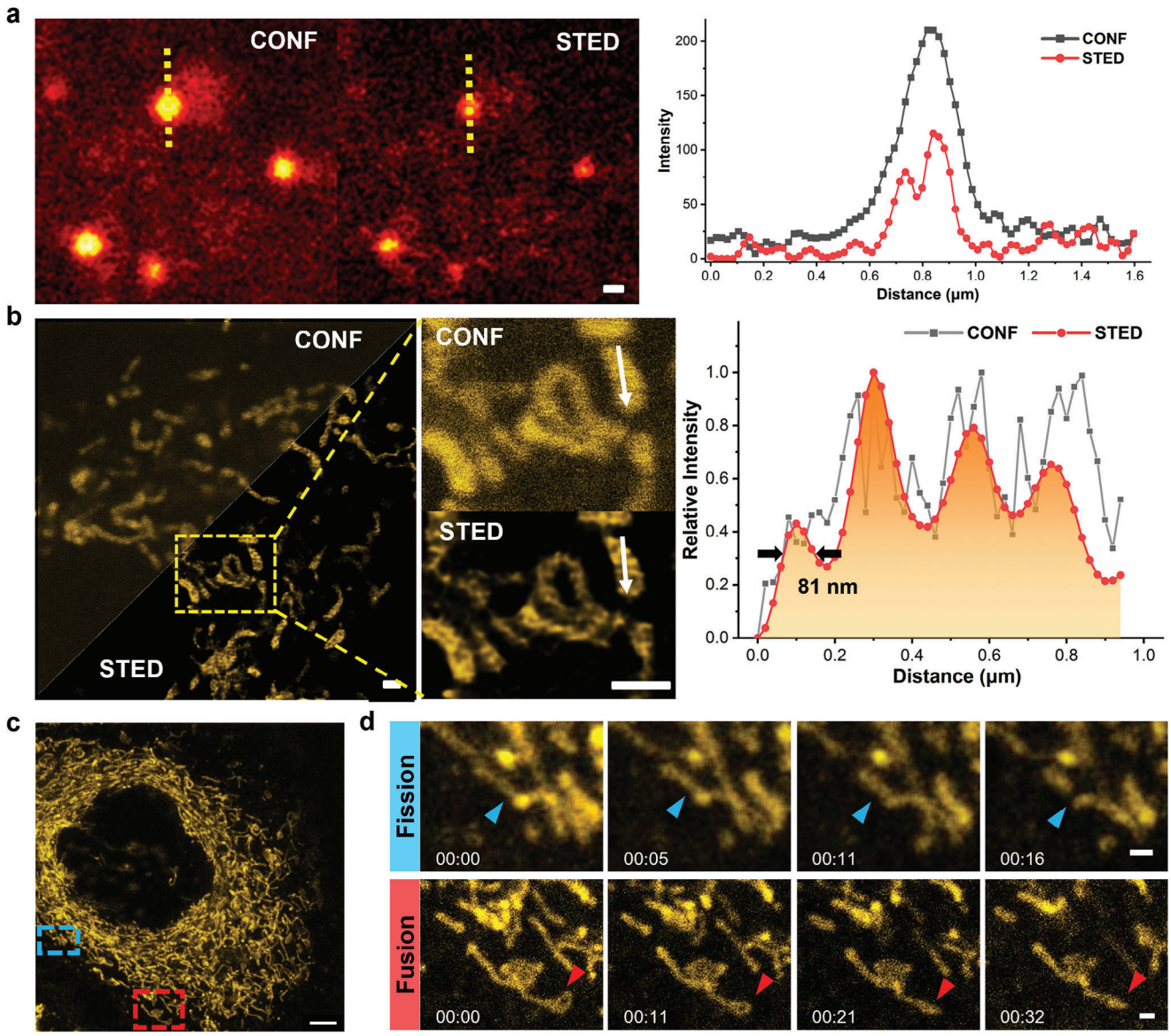

Figure 3. Live-cell mitochondrial STED imaging stained with MitoPDI-90. a) Local confocal (CONF) and STED imaging of living cells stained with MitoPDI-90 of high concentration (50 μM). The cross-section plot along the yellow dashed lines in the picture is shown. The scale bar is 100 nm. b) Local confocal and STED imaging of living cells stained with MitoPDI-90 of low concentration (5 μM). The cross-section plot along the white arrow in the picture is shown. The scale bar is 1 μm. c) STED time-lapse imaging of living cells stained with MitoPDI-90 (5 μM). The blue and red dashed boxes respectively select two local areas. The scale bar is 5 μm. d) Frame selection of time-lapse STED imaging of mitochondrial fission (blue dashed box, upper row) and fusion (red dashed box, lower row) in (c). The scale bar is 1 μm.

To quantify the change of MMP, the fluorescence intensity of living HeLa cells stained with Rho123, TMRM, and MitoPDI-90 was measured before and after the addition of 10 μM CCCP. By comparing the MMP levels before and after depolarization of mitochondria (Figure 4e), Rho123 showed a decrease of ≈30% and TMRM showed a decrease of ≈75%, while MitoPDI-90 exhibited a decrease of ≈42%, indicating that MitoPDI-90 has a sensitivity to MMP between Rho123 and TMRM. Notably, the fluorescence of MitoPDI-90, TMRM, and Rho123 could still be observed after cell apoptosis and collapse of MMP, albeit at a low intensity.[39] This might be because the recorded fluorescence signal comes from the entire cell, thus containing dye signals in the cytoplasm except for mitochondria. In general, the Rho123 suffers severe photobleaching during the image capture, which can lead to a decrease in signal. Therefore, the decline in MMP detected by MitoPDI-90 was more authentic and reliable than that observed with Rho123. Notably, Rhodamine derivatives used for MMP monitoring, such as Rho123, TMRM, and TMRE, have reversible binding to mitochondrial membranes, thus exhibiting a response to MMP.[20,39] Differently, the binding of NAO to the mitochondrial membrane is mostly irreversible and cannot respond to MMP.[25] Consequently, we speculate that the response of MitoPDI-90 to MMP indicates that their binding to the mitochondrial membrane is mostly reversible.

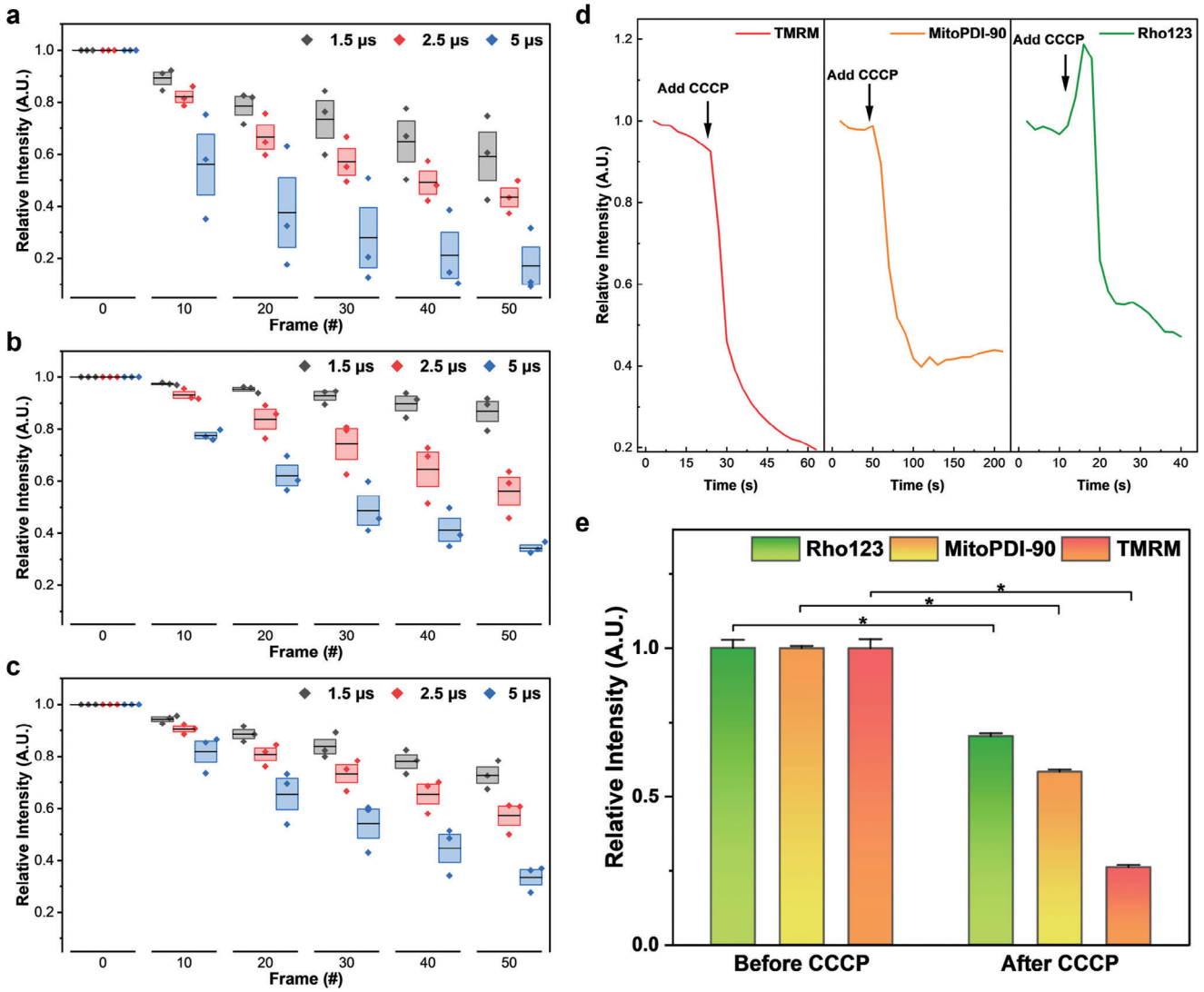

Figure 4. Comparison of MitoPDI-90, Rho123, and TMRM. The photobleaching resistance of a) Rho123, b) MitoPDI-90, and c) TMRM under different dwell times (1.5, 2.5, 5 μs). Imaging fluorescence intensity of Rho123, MitoPDI-90, and TMRM stained in living cells at different dwell times as a function of the number of frames, respectively. The box and the central line represent the mean ± SE, $n = 3$. d) The fluorescence intensity of MitoPDI-90 (5 μM), Rho123 (1.5 μM), and TMRM (20 nM) stained in living cells. The 10 μM CCCP was added to collapse MMP at the arrow. e) Statistical analysis of fluorescence intensity of MitoPDI-90, Rho123, and TMRM stained in living cells before and after CCCP application. The bar and the whisker represent the mean ± SE, $n = 15$. $^{*}p < 0.05$ compared with before the CCCP application.

Besides, the cytotoxicity of dyes is also an important property. Compared to Rho123, MitoPDI-90 has a smaller impact on overall cell activity (Figure S7, Supporting Information). More specifically, the impact of dyes on state 3 of mitochondria can be evaluated through mitochondrial oxygen consumption. Compared to TMRM, MitoPDI-90 of micromolar level concentration indeed causes inhibition of state 3, but the impact within the 20 μM range does not exceed 30% (Figure S8, Supporting Information). This may be related to the lower uptake of MitoPDI-90 by cells or mitochondria. Notably, rhodamine-based probes like Rho123 and TMRE can reduce respiratory rate and affect cell state after entering cells, and high concentrations of the dye accumulated can result in toxicity.[39,40]

2.5. STED Imaging and MMP Monitoring with MitoPDI-90

Further, the changes in MMP were observed under STED imaging to verify the multifunctional imaging ability of MitoPDI-90. Based on the heterogeneity of mitochondria, we speculate that intracellular mitochondria can also exhibit different MMP responses. To verify this hypothesis, the depolarization process of mitochondria was recorded using time-lapse STED imaging in living cells. Without additional stimuli, cells stained with MitoPDI-90 can be observed to undergo free morphological changes through STED imaging, while the fluorescence signal intensity remains almost unchanged (**Figure 5a**; Video S3, Supporting Information). The addition of CCCP (10 μM) induces

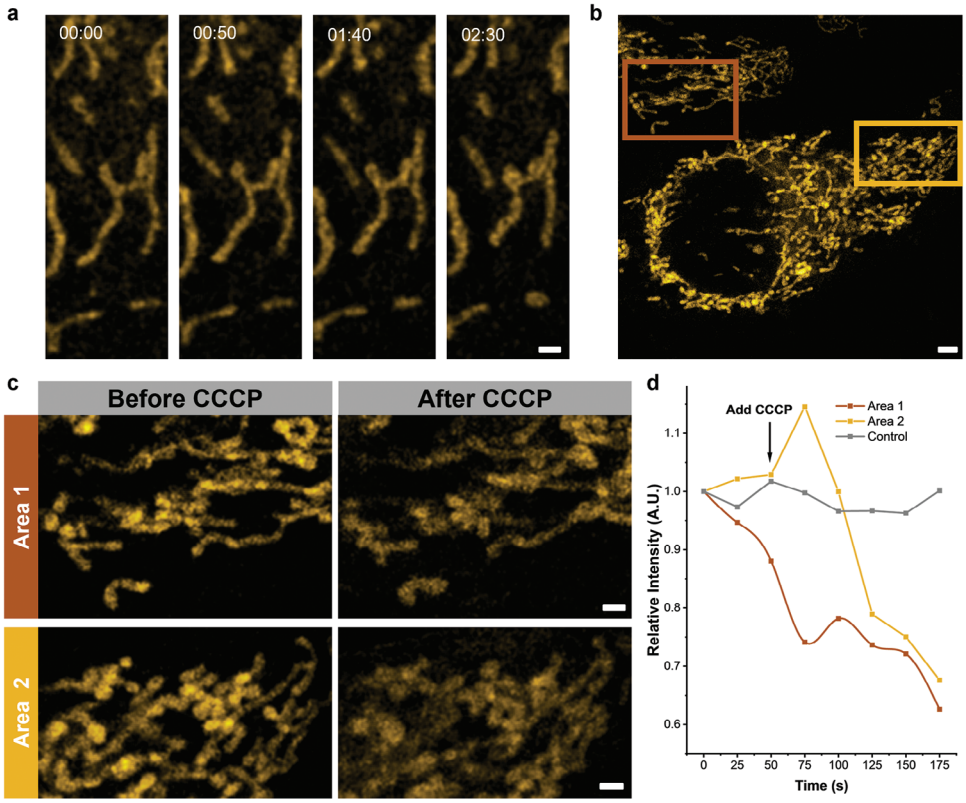

Figure 5. a) Frame selection of time-lapse STED imaging of living cells stained with MitoPDI-90 (5 μM). The scale bar is 1 μm. b) The time-lapse STED imaging of living cells stained with MitoPDI-90 (5 μM) during the depolarization of mitochondria. The brown and yellow boxes respectively select two local areas. The scale bar is 2 μm. c) The STED imaging of area 1 (brown box, upper row) and area 2 (yellow box, lower row) in (b). The scale bar is 1 μm. d) The average fluorescence intensity of MitoPDI-90 at the two areas in (b) is plotted as a function of the recorded frame number. The 10 μM CCCP was added to collapse MMP at the arrow. The average fluorescence intensity in (a) is used as a control.

MMP collapse, and this process is recorded through time-lapse STED imaging (Figure 5b,c; Video S4, Supporting Information). It can be seen that mitochondrial depolarization is accompanied by changes in mitochondrial morphology and a decrease in overall fluorescence intensity. Especially, it was also found that there were differences in the changes of MMP in local areas (Figure 5d), and different cells showed different MMP responses after adding CCCP. The results further confirm that MitoPDI-90 can achieve both super-resolution imaging and MMP monitoring simultaneously. Besides, mitochondria STED probes such as PKMO are not sensitive to changes in MMP (Figure S9, Supporting Information). Therefore, MitoPDI-90 can monitor changes in MMP while achieving STED imaging, thereby obtaining more information for the in situ study of mitochondrial functional activity.

3. Conclusion

In summary, MitoPDI-90 reported herein possessed high photostability, strong fluorescence emission, and low cell toxicity, making it suitable for super-resolution STED imaging of live-cell mitochondria and time-lapse imaging. Meanwhile, the cationic targeting mechanism of MitoPDI-90 enables dual imaging of structure and MMP for mitochondrial dynamics. Thus, MitoPDI-90 provided both super-resolution imaging and MMP monitoring capabilities, providing an elegant way to investigate the functional dynamics of mitochondria in living cells. We believe that MitoPDI-90, as a mitochondria probe for structure and function dual imaging, will provide further insight into the functional activity of mitochondria in living cells.

4. Experimental Section

Mitochondrial Labeling and Confocal Imaging: HeLa cells were seeded on glass-bottomed dishes before they were grown to a suitable density (24 h) via incubation in DMEM with 10% FBS (37 °C, 5% (v/v) CO_2). For the colocalization test, the cells were stained with 100 nM MitoBright LT Deep Red (MBDR, Dojindo) for 30 min and then with different concentrations of MitoPDI-90 (0, 1, 5, 20, 50, and 100 μM) for 20 min (37 °C). For the MMP test, the cells were stained with 1.5 μM Rho123 (Beyotime) or 5 μM MitoPDI-90 for ≈20 min (37 °C), then the medium was changed to fresh DMEM. As a comparison, the cells were stained with 20 nM TMRM (Adamas life) for 20 min, and then imaged with the dye stayed in the buffer. The confocal imaging was performed on Leica TCS SP8 STED 3× system equipped with a 100×/1.40 oil objective. The excitation light source was a white laser set to the following values: 480 nm (Rho123 channel),520 nm (MitoPDI-90 channel), 550 nm (TMRM channel), and 640 nm (MBDR channel). Emission light was set to the following spectral ranges: 500–550 nm (Rho123 channel), 540–620 nm (MitoPDI-90 channel), 565–650 nm (TMRM channel), and 655–700 nm (MBDR channel).

Live-Cell STED Imaging: HeLa cells were seeded on glass-bottomed dishes and stained in DMEM containing 5 μM MitoPDI-90 for 20 min in a

CO_2 incubator after incubation for 24 h. Then, the cells were washed three times with fresh medium to remove the free dye and kept in DMEM for imaging. The Leica TCS SP8 STED 3× system with 2 CW lasers at 592 and 660 nm and a pulsed laser at 775 nm with 80 MHz frequency for the depletion was used for STED imaging. An HyD detector and a STED WHITE objective (100×/1.40 Oil object) were employed. Unless otherwise noted, the STED images were acquired with excitation at 520 nm, emission in the range of 540–620 nm, and depletion at 775 nm. The images were processed using Fiji software.

Live-Cell Time-Lapse Imaging: Time-lapse confocal and STED imaging of the labeled cells were performed with the Leica TCS SP8 STED 3× system. In general, continuously capture 50 confocal images of stained cells with different dwell times to obtain videos.

Statistical Analysis: The fluorescence intensity was analyzed by using Fiji software. The co-localization coefficient was obtained via the "colocalization finder" plugin in ImageJ. The fluorescence intensity change curve, fluorescence intensity analysis, and co-localization coefficient statistics were all obtained with OriginPro 2023b software. Unless otherwise specified, all the data were denoted as mean ± SE. The *P*-values were calculated using a two-sided Student's *t*-test, $^{*}p < 0.05$.

Supporting Information

Supporting Information is available from the Wiley Online Library or from the author.

Acknowledgements

This work was supported by the National Key Research and Development Program of China (Grant No. SQ2021YFF0500363), the Natural Science Foundation of Shanghai (23 23ZR1433400), and the Shenzhen Science and Technology Innovation Program (JCYJ20210324123610030). The molecular synthesis of PDI probes was supported by Gentex Corporation Sponsorship under award #10060686. L.Z. has a significant financial interest in Gentex Corporation, which partially funded this research. The authors thank the Materials Characterization Center of East China Normal University for help with fluorescence imaging.

Conflict of Interest

L.Z. has a significant financial interest in Gentex Corporation, which partially funded this research.

Data Availability Statement

The data that support the findings of this study are available in the supplementary material of this article.

Keywords

cationic molecular, cristae, mitochondrial membrane potential, STED microscopy

Received: April 12, 2024
Revised: September 5, 2024
Published online: September 13, 2024

[1] H. Vakifahmetoglu-Norberg, A. T. Ouchida, E. Norberg, *Biochem. Biophys. Res. Commun.* **2017**, *482*, 426.
[2] S. Cogliati, J. A. Enriquez, L. Scorrano, *Trends Biochem. Sci.* **2016**, *41*, 261.
[3] W. Kühlbrandt, *BMC Biol.* **2015**, *13*, 89.
[4] T. Stephan, A. Roesch, D. Riedel, S. Jakobs, *Sci. Rep.* **2019**, *9*, 12419.
[5] Y. Kiriyama, H. Nochi, *Cells.* **2018**, *7*, 95.
[6] S. Jakobs, S. Stoldt, D. Neumann, in *High Resolution Microbial Single Cell Analytics*, (Eds: S. Müller, T. Bley), Springer, Berlin, Heidelberg **2011**, pp. 1–19.
[7] G. G. Wolken, E. A. Arriaga, *Anal. Chem.* **2014**, *86*, 4217.
[8] N. Esteras, M. J. W. Adjobo-Hermans, A. Y. Abramov, W. J. H. Koopman, *Methods Cell Biol.* **2020**, *155*, 221.
[9] C. Wang, M. Taki, Y. Sato, Y. Tamura, H. Yaginuma, Y. Okada, S. Yamaguchi, *Proc. Natl. Acad. Sci. U S A.* **2019**, *116*, 15817.
[10] X. Yang, Z. Yang, Z. Wu, Y. He, C. Shan, P. Chai, C. Ma, M. Tian, J. Teng, D. Jin, W. Yan, P. Das, J. Qu, P. Xi, *Nat. Commun.* **2020**, *11*, 3699.
[11] L. Shao, P. Kner, E. H. Rego, M. G. L. Gustafsson, *Nat. Methods.* **2011**, *8*, 1044.
[12] F. Bottanelli, E. B. Kromann, E. S. Allgeyer, R. S. Erdmann, S. W. Baguley, G. Sirinakis, A. Schepartz, D. Baddeley, D. K. Toomre, J. E. Rothman, J. Bewersdorf, *Nat. Commun.* **2016**, *7*, 10778.
[13] R. Fiolka, L. Shao, E. H. Rego, M. W. Davidson, M. G. L. Gustafsson, *Proc. Natl. Acad. Sci. USA.* **2012**, *109*, 5311.
[14] S. J. Sahl, F. Balzarotti, J. Keller-Findeisen, M. Leutenegger, V. Westphal, A. Egner, F. Lavoie-Cardinal, A. Chmyrov, T. Grotjohann, S. Jakobs, *Science.* **2016**, *352*, 527.
[15] M. V. Sednev, V. N. Belov, S. W. Hell, *Methods Appl. Fluoresc.* **2015**, *3*, 042004.
[16] A. Stockhammer, F. Bottanelli, *J. Phys. D: Appl. Phys.* **2020**, *54*, 033001.
[17] B. Huang, H. Babcock, X. Zhuang, *Cell.* **2010**, *143*, 1047.
[18] R. Xu, D. Dang, Z. Wang, Y. Zhou, Y. Xu, Y. Zhao, X. Wang, Z. Yang, L. Meng, *Chem. Sci.* **2022**, *13*, 1270.
[19] Y. Xu, R. Xu, Z. Wang, Y. Zhou, Q. Shen, W. Ji, D. Dang, L. Meng, B. Z. Tang, *Chem. Soc. Rev.* **2021**, *50*, 667.
[20] C. Lee, D. C. Wallace, P. J. Burke, *ACS Nano.* **2024**, *18*, 1345.
[21] Y. Xu, D. Dang, N. Zhang, J. Zhang, R. Xu, Z. Wang, Y. Zhou, H. Zhang, H. Liu, Z. Yang, L. Meng, J. W. Y. Lam, B. Z. Tang, *ACS Nano.* **2022**, *16*, 5932.
[22] T. Liu, T. Stephan, P. Chen, J. Keller-Findeisen, J. Chen, D. Riedel, Z. Yang, S. Jakobs, Z. Chen, *Proc. Natl. Acad. Sci. USA.* **2022**, *119*, e2215799119.
[23] J. Jacobson, M. R. Duchen, S. J. R. Heales, *J. Neurochem.* **2002**, *82*, 224.
[24] L. D. Zorova, V. A. Popkov, E. Y. Plotnikov, D. N. Silachev, I. B. Pevzner, S. S. Jankauskas, V. A. Babenko, S. D. Zorov, A. V. Balakireva, M. Juhaszova, S. J. Sollott, D. B. Zorov, *Anal. Biochem.* **2018**, *552*, 50.
[25] D. M. Wolf, M. Segawa, A. K. Kondadi, R. Anand, S. T. Bailey, A. S. Reichert, A. M. van der Bliek, D. B. Shackelford, M. Liesa, O. S. Shirihai, *EMBO J.* **2019**, *38*, 101056.
[26] C. Ji, W. Cheng, Q. Yuan, K. Müllen, M. Yin, *Acc. Chem. Res.* **2019**, *52*, 2266.
[27] Z. Yang, X. Chen, *Acc. Chem. Res.* **2019**, *52*, 1245.
[28] S. Chen, P. Slattum, C. Wang, L. Zang, *Chem. Rev.* **2015**, *115*, 11967.
[29] S. Chen, Z. Xue, N. Gao, X. Yang, L. Zang, *Sensors.* **2020**, *20*, 917.
[30] J. Zielonka, J. Joseph, A. Sikora, M. Hardy, O. Ouari, J. Vasquez-Vivar, G. Cheng, M. Lopez, B. Kalyanaraman, *Chem. Rev.* **2017**, *117*, 10043.
[31] X. Guo, N. Yang, W. Ji, H. Zhang, X. Dong, Z. Zhou, L. Li, H.-M. Shen, S. Q. Yao, W. Huang, *Adv. Mater.* **2021**, *33*, 2007778.
[32] F. Würthner, C. R. Saha-Möller, B. Fimmel, S. Ogi, P. Leowanawat, D. Schmidt, *Chem. Rev.* **2016**, *116*, 962.
[33] K. Balakrishnan, A. Datar, T. Naddo, J. Huang, R. Oitker, M. Yen, J. Zhao, L. Zang, *J. Am. Chem. Soc.* **2006**, *128*, 7390.

[34] A. N. Butkevich, G. Yu Mitronova, S. C. Sidenstein, J. L. Klocke, D. Kamin, D. N. H. Meineke, E. D'Este, P.-T. Kraemer, J. G. Danzl, V. N. Belov, S. W. Hell, *Angew. Chem., Int. Ed.* **2016**, *55*, 3290.
[35] K. L. Cerveny, Y. Tamura, Z. Zhang, R. E. Jensen, H. Sesaki, *Trends Cell Biol.* **2007**, *17*, 563.
[36] J. D. Ly, D. R. Grubb, A. Lawen, *Apoptosis.* **2003**, *8*, 115.
[37] S. W. Perry, J. P. Norman, J. Barbieri, E. B. Brown, H. A. Gelbard, *BioTechniques.* **2011**, *50*, 98.
[38] D. G. Nicholls, S. J. Ferguson, in *Bioenergetics*, 4th ed. (Eds: D. G. Nicholls, S. J. Ferguson), Academic Press, Boston **2013**, pp. 255–302.
[39] R. C. Scaduto, L. W. Grotyohann, *Biophys. J.* **1999**, *76*, 469.
[40] T. J. Lampidis, C. Salet, G. Moreno, L. B. Chen, *Agents Actions.* **1984**, *14*, 751.